Evaluation of Bosch Process–Sourced Carbon in Low-Carbon Steel and Gray Iron Casting for Martian Surface Manufacturing

Blake C. Stewart[1]; Haley R. Doude, Ph.D.[2]; Terry L. Taylor[3];
Morgan B. Abney, Ph.D.[4]; and Hongjoo Rhee, Ph.D.[5]

Abstract: As research continues for the first crewed missions to and the eventual colonization of Mars, the need for materials for construction of structural and mechanical components remains paramount. The use of in situ resource utilization (ISRU) techniques is critical due to the financial and physical burdens of sending supplies beyond low-Earth orbit. The Bosch process is currently in development as a life-support system at National Aeronautics and Space Administration (NASA) Marshall Space Flight Center (MSFC) to regenerate oxygen (O_2) from metabolic carbon dioxide (CO_2) with the by-product of elemental carbon (C). In this study, the use of this novel C source for alloying with iron (Fe) to produce ferrous alloys was studied to determine if the Bosch-sourced C could provide similar metallurgical results to a traditional C source. The Bosch C was produced by MSFC through their C-formation reactor (C-Fr) using mill scale (Fe_3C) as the reaction catalyst. Two types of ferrous alloys were manufactured using the Bosch-sourced C and a control source C. Mechanical and microstructural properties obtained from each equivalent grade revealed comparable metallurgical results. **DOI: [10.1061/(ASCE)AS.1943-5525.0001394](https://doi.org/10.1061/(ASCE)AS.1943-5525.0001394).** © 2021 American Society of Civil Engineers.

Introduction

With the race to return to the Lunar surface and the future landing on Mars, in situ resource utilization (ISRU) technology will enable expanded exploration and colonization beyond low-Earth orbit. Due to the inhospitable environment on these extraterrestrial bodies, numerous mechanical and structural components will be required, and these must be manufactured from local resources. Currently, it is estimated that the cost of shipping cargo to the International Space Station (ISS) is as much as around $94,800 per kilogram ($43,000 per pound) ([Kramer and Mosher 2016](#)). Even with the ambitious estimates by SpaceX, the plans for their Starship estimate roughly $145 per kilogram ($66 per pound) for Lunar deliveries, assuming regular launches and full payloads ([Zafar 2020](#)). The average distance to the moon is approximately

[1]Graduate Research Assistant, Center for Advanced Vehicular Systems, P.O. Box 5405, Mississippi State, MS 39762; Ph. D. Candidate, Dept. of Mechanical Engineering, Mississippi State Univ., P.O. Box 9552, Mississippi State, MS 39762. Email: bcs346@msstate.edu

[2]Assistant Research Professor, Center for Advanced Vehicular Systems, P.O. Box 5405, Mississippi State, MS 39762. Email: haley@cavs.msstate.edu

[3]Technology Transfer Office Manager, Marshall Space Flight Center, National Aeronautics and Space Administration, Martin Rd. SW, Huntsville, AL 35808. ORCID: https://orcid.org/0000-0002-6765-3765. Email: terry.taylor@nasa.gov

[4]Environmental Control and Life Support System Technical Fellow, Marshall Space Flight Center, National Aeronautics and Space Administration, Martin Rd. SW, Huntsville, AL 35808. Email: morgan.b.abney@nasa.gov

[5]Associate Director, Center for Advanced Vehicular Systems, P.O. Box 5405, Mississippi State, MS 39762; Associate Professor, Dept. of Mechanical Engineering, Mississippi State Univ., P.O. Box 9552, Mississippi State, MS 39762 (corresponding author). Email: hrhee@me.msstate.edu

383,000 km (238,000 mi) away ([Erickson and Doyle 2019](#)), with Mars being an astronomical 234.5 million km (145.74 million mi) ([NASA 2020](#)). Extrapolating these costs for future Martian deliveries, this payload cost increases to $88,850 per kilogram ($40,300 per pound); however, this cost is likely to be much greater due to the disparity in travel distance and technology required. These costs are not feasible for substantial colonization missions; therefore, a local manufacturing operation must be developed to construct the habitats and equipment that will be required for survival.

Besides the cold climate on the Martian surface, the atmosphere is not hospitable to human life. Data from the Curiosity rover showed the atmosphere is approximately 96% CO_2, with trace amounts of argon (Ar), nitrogen (N_2), carbon monoxide (CO), and a small amount of $O_2(1.45\% \pm 0.09\%)$ ([Mahaffy et al. 2013](#)). Currently studied at National Aeronautics and Space Administration (NASA) Marshall Space Flight Center (MSFC) is the Bosch process for use as a life support system for O_2 regeneration with the by-product of pure C(s). The Bosch process is also a closed-loop system with the only inputs required being CO_2 and the output of O_2 and C [assuming electrolysis of Bosch product water (H_2O)]. This process is the combination of three reactions: the reverse water-gas shift (RWGS) reaction, CO hydrogenation, and Boudouard reactions, as shown in Eqs. (1)–(3). The summarized Bosch process is shown in Eq. (4) ([Abney et al. 2013](#))

$$CO_2 + H_2 \leftrightarrow H_2O + CO \tag{1}$$

$$CO + H_2 \leftrightarrow H_2O + C(s) \tag{2}$$

$$2CO \leftrightarrow CO_2 + C(s) \tag{3}$$

$$CO_2 + 2H_2 \leftrightarrow 2H_2O + C(s) \tag{4}$$
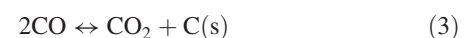
The Bosch process is limited by the C-formation reactions shown in Eqs. (2) and (3), as well as the life of the catalyst ([Abney and Mansell 2011](#)). The C-Fr at MSFC is currently capable of producing C at a rate of over 8 g/h. The Bosch process has been previously applied in the cement industry to reduce oxocarbon

emissions as well as using the captured C as an additive in cement (Abney et al. 2016).

Not only does the Bosch process enable the recovery and recycling of metabolic O_2 from astronauts, but the reactor could potentially be a means to provide oxygen for a small habitat on the surface of Mars, and a larger reactor could recycle CO_2 emissions from manufacturing centers and the native atmosphere with the C by-product used in material construction. A larger reactor could additionally provide the oxidant for propellant to return people and shipments back off the Martian surface.

One surface manufacturing capability that would benefit from the Bosch process is Martian steel manufacturing. In situ production of steel would provide the capability to produce structural and mechanical components on the surface of Mars with the local resources, requiring only minimal equipment being launched from Earth. This approach has the obvious benefits of providing a means to efficient manufacturing capability on the Mars surface, as well as reducing the cost of colonization. Developing the capabilities in situ will significantly increase the likelihood of success of the colonies and allow them to thrive in their new environment.

Using the idea, the C emissions from Martian steel manufacturing could be converted using the Bosch process system to obtain H_2O and a C(s) by-product. This approach has the obvious benefits of (1) recycling carbon feed stock for steel production, and (2) producing water as a usable by-product instead of CO_2. NASA's interest in the Bosch process for a life-support system presents a secondary benefit of utilizing the C by-product as a primary alloying element within steelmaking. This enables NASA to produce steel in situ on the surface of extraterrestrial bodies, allowing for endless possibilities for future Martian or Lunar colonies to thrive.

A study has recently been released that allowed researchers to generate coal from CO_2, similar to the benefits of the Bosch process (Esrafilzadeh et al. 2019). Commercially, this Bosch technology could potentially be used to recycle emissions from a blast furnace, enabling a steel manufacturer to reduce or eliminate the purchase of elemental C (metallurgical coke) for alloying later in the steelmaking process, similar to the aforementioned cement industry; however, this is outside the scope of the work shown hereafter.

This paper seeks to evaluate the feasibility of in situ steel production using carbon sourced from the Bosch reaction by demonstrating similar metallurgical results to a traditional commercially available alloying C source.

Materials and Methods

For this study, two ferrous alloys were manufactured: one based on American Iron and Steel Institute (AISI) 1020 steel, the other based on gray cast iron, where both alloys were produced using C from two different sources: conventional metallurgical coke (control C, 99% purity) and the Bosch C (93% average purity, Fe_3C mill scale balance) sourced from NASA's C-Fr at MSFC. All other elements [Fe, silicon (Si), and manganese (Mn)] were commercially sourced with 99% + purity. A high-frequency, high-vacuum induction melting furnace (VIMF) manufactured by Dongyang IMF (Incheon, South Korea) was used to melt and cast the alloys. A total of 12 ingots were cast at 20 kg (44 lb) each to produce six low-C steel ingots and six cast-iron ingots. Out of six ingots from each grade, three were produced using the control C and the other three were manufactured using Bosch C, as shown in Fig. 1.

The alloying elements were added to the crucible before heating with the C wrapped in a small tissue pouch to prevent C from being pulled into the vacuum pumps during depressurizing to 1.3×10^{-4} Pa (10^{-6} torr), followed by the argon backfill. The furnace was then
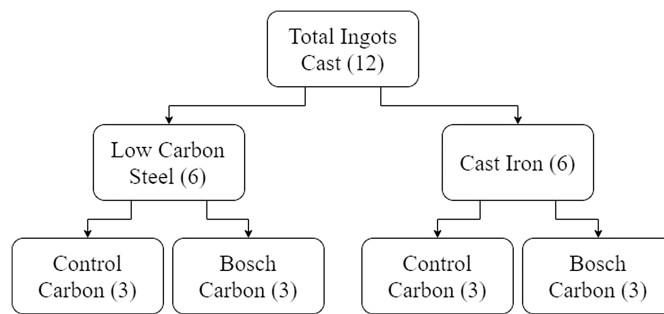
Fig. 1. Flowchart of cast alloys. Diagram shows two alloys with two carbon sources, with three iterations each for a total of 12 ingots cast.

ramped in 10-kW intervals at 10 min each until 60 kW is applied and full melting occurs. The melt was induction-stirred for 10 min before ramping down the applied power to cool the melt to a temperature of 1,400°C–1,450°C, and then poured into a 5.08-cm (2-in.)-thick cast-iron two-piece mold with 25.4 cm (10 in.) length and 20.32 cm (8 in.) width. After the ingot was cooled to ambient temperature, the ingot was removed from the VIMF and mold. The top 2.5 cm (1 in.) of each ingot was discarded to remove potential casting porosity and any possible slag.

Before reheating and hot rolling, a Sentrotech (ST-1500C-161622, Strongsville, Ohio) box furnace was used to fully austenitize and soften the low-C steel ingots at 1,250°C in an argon-purged environment to prevent surface oxidation during reheating. A Fenn (4-125) 2 hi/4 hi reversing rolling mill with 30.48 cm (12 in.) diameter and 38.1 cm (15 in.) face width rolls was used to hot roll the low-C steel from 5.08-cm (2-in.)-thick ingots to 1.27-cm (0.5-in.)-thick plates. The cast-iron ingot samples were tested in the as-cast condition.

Carbon Analysis

Prior to casting these alloys, the C obtained from the different sources were compared using the X-ray powder diffraction (XRD) technique with a Rigaku Ultima III X-ray diffractometer (Tokyo) to determine the allotropy of the samples. The control C was ground to a fine powder using a mortar and pestle for XRD analysis. Due to the fine consistency of the Bosch C, grinding was not required. The as-received C sources can be seen in Fig. 2. The powders were mounted in 0.5-mm-deep glass slides and analyzed using a copper K-α wavelength between 10° and 90°.

A JEOL 6500 (Peabody, Massachusetts) field emission gun scanning electron microscope (FEG-SEM) was used to observe the morphology and relative size of C sources. Each sample was poured on 1.27-cm (0.5-in.) aluminum specimen mounts with carbon tape, and an air duster was used to remove excessive powders.

Steel and Cast-Iron Characterization

Chemical Composition
Chemical compositions of produced steel plates and cast-iron ingots were analyzed using a Spectro Spectromaxx spectrometer (Kleve, Germany), which uses optical emission spectrometry (OES). After rolling the low-C steel ingots, OES measurements were taken 5.08 cm (2 in.) from the edge of the rolled plates. For the cast-iron ingots, the bottom 2.54 cm (1 in.) of the ingot was cut and used for chemical analysis. For more accurate C and sulfur (S) composition values, a LECO CS744 carbon/sulfur analyzer (St. Joseph, Michigan) was also used due to its specialized, separate nondispersive infrared cells for SO_2 and CO_2 from the combustion of the samples.
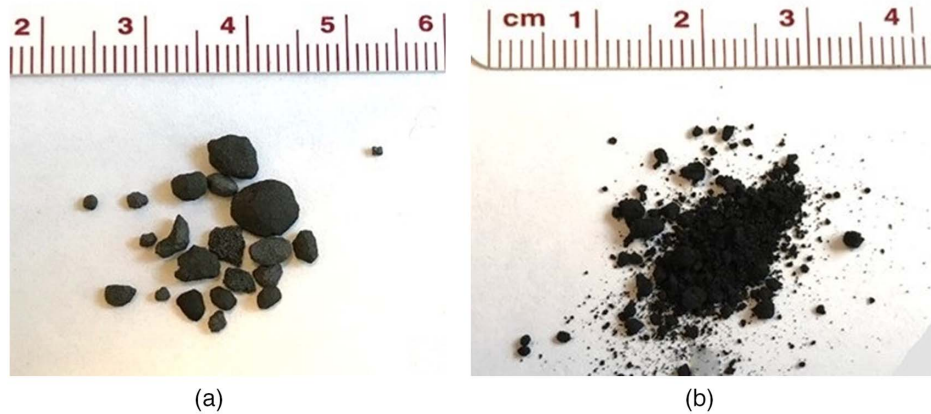
Fig. 2. As-received carbon sources: (a) commercial C; and (b) Bosch C.
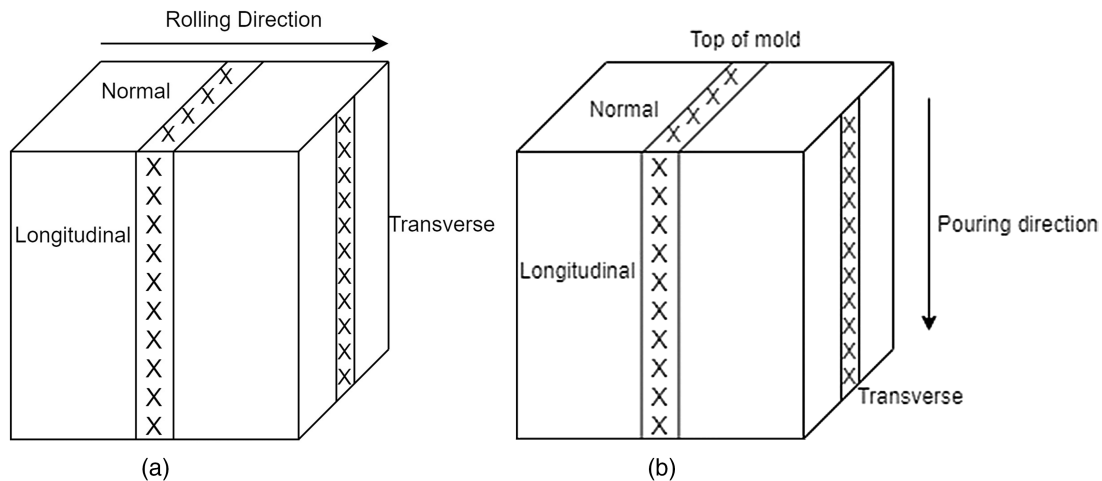
Fig. 3. Micrograph orientations: locations for (a) low-C steel alloy plates; and (b) gray cast-iron ingots.

Grain Structure

For microstructural investigations, metallographic samples were cut from the orientations shown in Fig. 3, and three-dimensionally represented. With each sample, 2% nitric acid etchant was used and optical micrographs were taken to visualize the grain structure of each material with a Zeiss Axiovert 200M optical microscope (Oberkochen, Germany).

The average phase fraction for the low-C steel plates was found using a contrast particle function in ImageJ software, and the average grain size was calculated using the Planimetric (Jefferies) procedure in accordance with ASTM E112-13 (ASTM 2013). Three images from each of the three views for each casting were used to determine the average grain size.

Mechanical Testing

Mechanical testing included tension, compression, and hardness (Brinell and Rockwell) tests. Tensile and compressive test specimens were machined by using a wire-cut electrical discharge machine (wire-EDM). Tensile samples were obtained from both the rolling direction and transverse direction for the low-C steel plates. For the cast-iron ingots, tensile samples were obtained in the normal and pouring directions. The tensile specimen dimensions were in accordance with ASTM E8 (ASTM 2016) subsize specimen [0.635 cm outer diameter (OD) (0.25 in.)], and compressive specimens, in accordance with ASTM E9 (ASTM 2019b), were

10 mm in diameter and 10-mm-long cylinders. All testing was performed on an Instron 5882 electromechanical frame (Norwood, Massachusetts) using a 100-kN load cell with elongation measured with an Instron 25-mm extensometer (Norwood, Massachusetts).

The tests were strain controlled at $0.001~\text{s}^{-1}$ until failure for tensile or up to 80% of load cell capacity for compressive tests. This end test criteria allowed for a sufficient length of test for a determination of ductile or brittle material failure based on a load drop off after yielding or sudden shatter. Fractography was then performed on the failed tensile specimens under a Ziess Supra40 FEG-SEM (Oberkochen, Germany) to observe the tensile fracture surfaces.

Brinell hardness tests were carried out with a King Brinell tester, and a LECO LR-300TD Rockwell (Phoenixville, Pennsylvania) hardness tester was used for Rockwell-B and Rockwell-C (cast iron only) scale hardness tests.

Results and Discussion

Carbon Analysis

The XRD results obtained from both C sources are shown in Fig. 4. From the Bosch C source, there is a well-defined peak at 26.4°, indicating orthorhombic graphite (94.2% by weight). There is also a small peak at 44.6° of an orthorhombic cohenite (Fe_3C) (5.8%
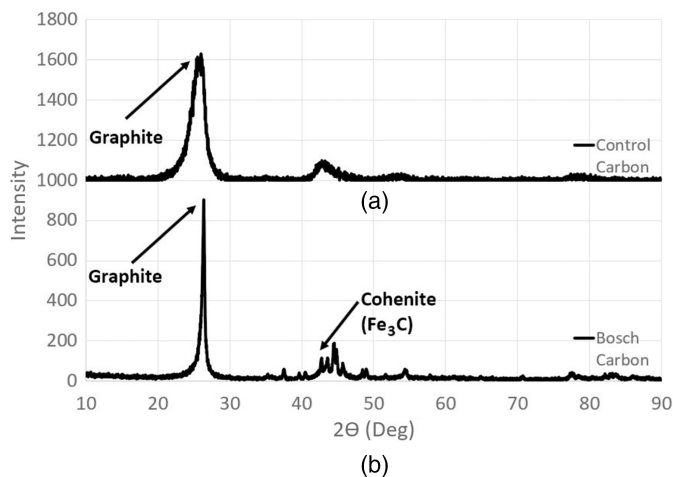
Fig. 4. Carbon sample XRD plots: comparison of (a) conventional; and (b) Bosch C sources.

by weight) (Devi and Kannan 2007). The control carbon source showed a slightly broadened, shifted orthorhombic graphite peak at 26.1°.

The characteristic graphite peak is at 26.7° 2Θ. The Bosch C source was very close with an undistorted peak. The conventional C showed a slightly shifted and broadened peak. Shifted and broadened XRD peaks are attributed to uniform and nonuniform strain in the lattice structure of the material (Cullity and Stock 1978). Because the control C sample had to be ground before being loaded into the sample slide, this is likely the cause of the peak alteration. The C-Fr used to generate the Bosch C uses an Fe_3C catalyst that was not filtered from the Bosch C prior to casting in the VIMF. This is the source of the Fe_3C in the Bosch C XRD scan.

SEM images showed that the control C consists of groups of spherical particles approximately 80–150 μm in diameter, as shown in Fig. 5(a), and the Bosch C is formed into irregularly shaped, smaller particles with a fuzzy exterior, in formations approximately 10–75 μm in diameter [Fig. 5(b)].

The two different C sources show most of their differences in their morphologies. However, when used as the C source for the

material melt in the furnace at temperatures exceeding 1,600°C, both sources seem to diffuse into the material similarly. It was noticed that the Bosch C, due to its fine texture and large volume, tended to float to the top of the melt and required more manual stirring in the high-C cast-iron application. Preliminary results by the authors (Rhee, et al., unpublished data, 2017) predating this study indicated a potentially lower diffusion rate in the conventional C due to its large particle size, resulting in C segregation in higher C steel alloys; however, with adequate stir time, C segregation was not a further issue.

Steel and Cast-Iron Characterization

Chemical Composition

The chemical composition results obtained from produced steel alloys are depicted in Table 1. Purity of each C source was considered along with carbon recovery [96% recovery based on previous castings at Mississippi State University (MSU)] during melting to ensure the appropriate amount of C was added to the crucible in the VIMF.

Chemical composition of each respective material was verified to be within the desired range for most (ASTM 2018). It was found that the Si content of the second control C cast-iron ingot was slightly lower than the other cast-iron ingots (2.01% versus ~2.5% by weight); however, the effects from the Si composition disparity were negligible and did not result in a measurable deviation in comparison with other results. The C in the third Bosch C cast-iron ingot was also significantly lower (2.88% versus ~3.50% by weight), but again the C quantity deviation does not affect the results significantly ($p < 0.05$).

The target Mn composition was 0.45% by weight in all castings. The Mn recovery rate in the VIMF was observed to be slightly higher than expected. The control C cast-iron ingots cast resulted in an average of approximately 0.58% by weight Mn. Before the Bosch C cast-iron ingots were cast, the Mn recovery rate was adjusted in the charge calculation, resulting in a lower mean Mn composition (0.491% by weight) for the Bosch C cast iron. It was also noted that the S content was slightly higher in the control C low-carbon steel plates, and significantly higher in the control C cast iron. The S content was comparable in both low-C steel and cast-iron Bosch C samples. This indicates that the primary S source was the conventional C used.
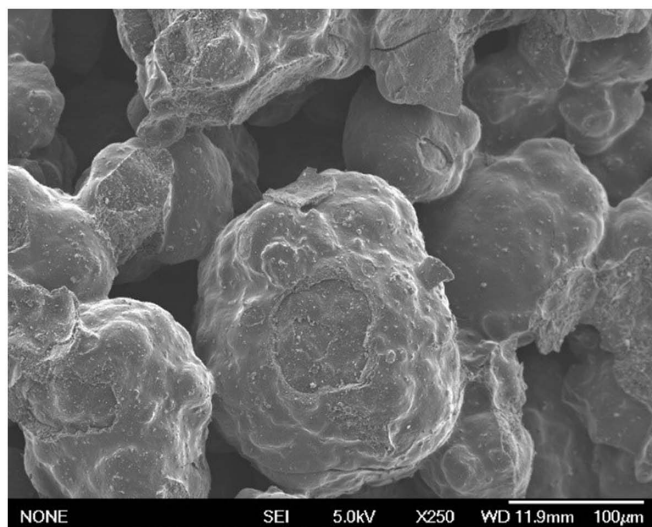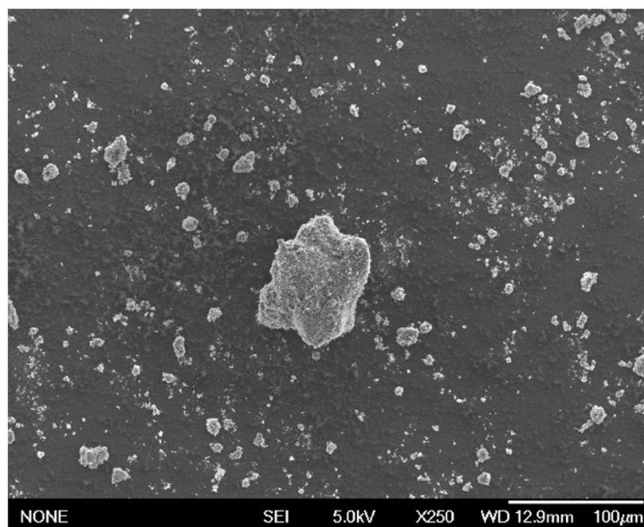
Fig. 5. SEM micrographs of carbon sources: (a) conventional C; and (b) Bosch C.

Table 1. Chemical compositions of produced steel alloys

Steel alloys and C source	Ingot ID	Chemical composition (% by weight)					
		C	Si	Mn	P	S	Fe
Low-carbon steel, conventional C	Target (ASTM A830/A830M-18)	0.20	—	0.45	—	—	Balance
	1	0.183	0.009	0.489	0.0038	0.0113	99.18
	2	0.206	0.011	0.508	0.0070	0.0110	99.10
	3	0.180	0.110	0.499	0.0071	0.0098	99.14
Low-carbon steel, Bosch C	Target (ASTM A830/A830M-18)	0.20	—	0.45	—	—	Balance
	1	0.203	0.035	0.516	0.0068	0.0044	99.06
	2	0.188	0.020	0.498	0.0067	0.0025	99.10
	3	0.191	0.007	0.506	0.0046	0.0016	99.12
Cast iron, conventional C	Target (Radzikowska 2004)	3.50	2.50	0.45	—	—	Balance
	1	3.20	2.45	0.592	0.0036	0.1369	92.76
	2	3.39	2.01	0.566	0.0035	0.1453	92.58
	3	3.41	2.56	0.583	0.0034	0.1343	92.40
Cast iron, Bosch C	Target (Radzikowska 2004)	3.50	2.50	0.45	—	—	Balance
	1	3.40	2.60	0.485	0.0031	0.0041	92.94
	2	3.55	2.61	0.510	0.0044	0.0021	92.98
	3	2.88	2.39	0.479	0.0064	0.0099	90.27

Grain Structure

Microstructures obtained from the low-C steel plates are shown in Fig. 6. Both C sources produced similar microstructure of ferrite grains (white) with small amounts of pearlite (black) between. Average grain size was also similar, with the exception of the second control low-C steel plate. This plate exhibited a slightly smaller grain size with elongated grains in the rolling direction. The average phase fractions and grain sizes are given in Table 2.

The images taken from the cast-iron samples were characterized in accordance with ASTM A247 (ASTM 2019a) by the graphite in the casting. All samples resembled most closely Distribution D, Class 7 microstructure. Although the first and second control C cast-iron ingots showed a slight variance in the etched microstructure in some areas, the most representative of each C source cast-iron microstructure is shown in Fig. 7.

The refined, elongated grain structure of the second control low-C steel plate is likely due to a lower-temperature rolling scenario. There were feeding issues into the rolling mill, giving more time for the plate to cool before rolling was complete; therefore, the grains were elongated rather than refined. The differences in cast-iron microstructures can likely be attributed to different cooling rates throughout the ingot after casting. The size and shape of the mold, as well as pouring speed, could result in a nonhomogeneous microstructure across the ingots. Cast iron grain structure is highly dependent on
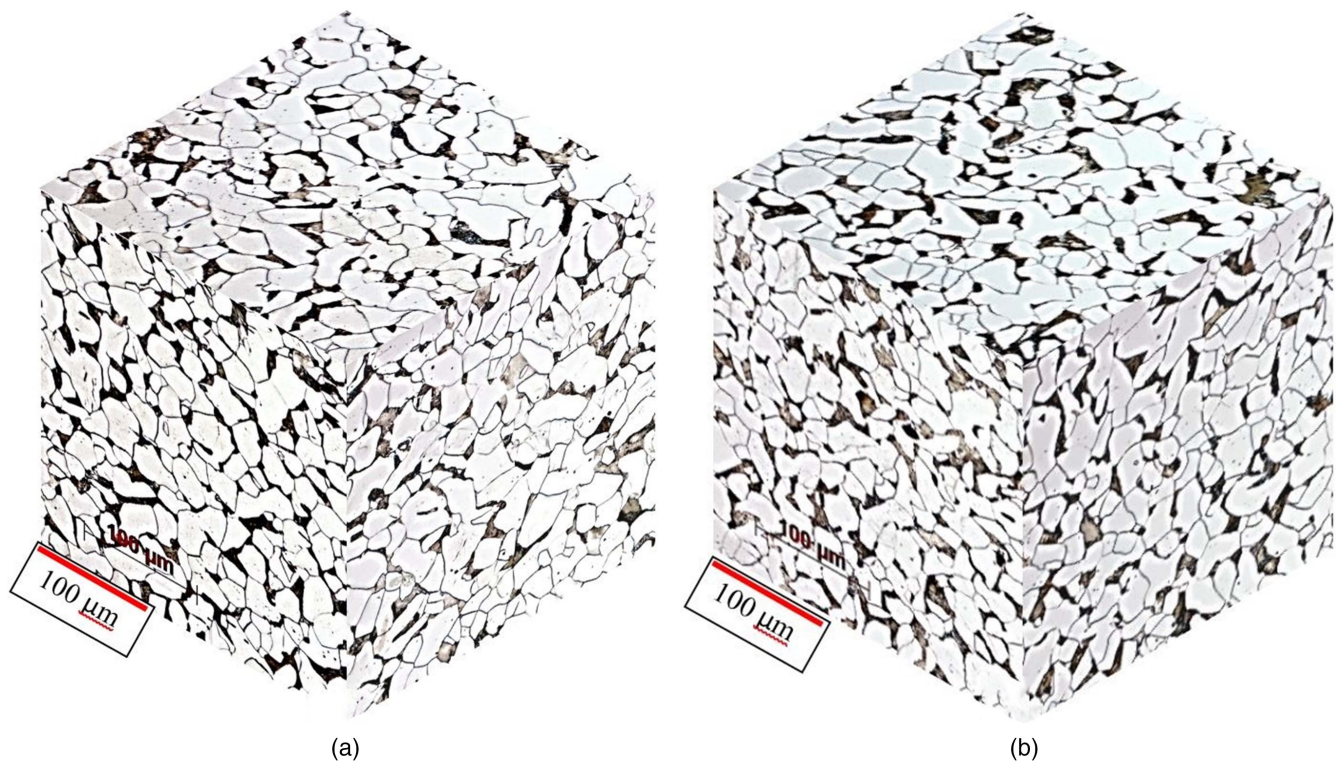
Fig. 6. Three-dimensional images constructed from two-dimensional micrographs of low-C steel alloys using: (a) control carbon source; and (b) Bosch C source.

Table 2. Phase fraction and grain size of produced low-C steels and graphite grain structure of produced gray cast iron

	Phase fraction		Grain size (μm)
Alloy steels and C source	Ferrite (%)	Pearlite (%)	
Low-carbon steel, conventional C	82.6 ± 1	17.4 ± 1	33.4 ± 5
Low-carbon steel, Bosch C	81.7 ± 0.6	18.3 ± 0.6	36.6 ± 2
Cast iron, conventional C	Distribution D, Class 7		—
Cast iron, Bosch C			

cooling rate (Davis 1996). A simple normalization or annealing process on the ingots would homogenize the ingots; however, the material was desired to be tested in the as-cast condition. Overall, a similar dendritic structure is observed in all the cast iron iterations.

Mechanical Testing

The stress-strain curves for all low-C steel specimens are shown in Fig. 8, and the cast-iron tensile curves are shown in Fig. 9, respectively, with data from each curve given in Table 3. Tensile stress-strain plots obtained from low-C steels revealed the effects of Lüder's bands leading to the yield point phenomenon. All low-C steel tensile test results showed comparable yield phenomena and flow stress behavior and are all within a reasonable deviation from each other. Cast-iron samples revealed some variance as expected; however, each respective ingot is consistent within itself.

These tensile stress-strain curves are common for low-C steel (Dieter 1986) and are consistent for each sample. Although the second control low-C steel plate in the transverse direction has a significantly higher upper yield stress, this is easily explained by its smaller grain size. Per the Hall-Petch relationship of grain size to yield stress (Smith and Hashemi 2006), this is expected. Overall, all

tensile testing, including both directions, for low-C steels show only 22.5 MPa standard deviation for the upper yield stress (12.5 MPa for lower yield stress). The elongation in the gauge section for all samples is also very similar (40.7% ± 2.7%) with the difference between conventional and Bosch C alloys being statistically insignificant. This implies that both C sources show similar mechanical behavior under tension for the low-C steel alloy. The yield and ultimate stresses as well as the elongation at failure are higher than the accepted value for 1020 steel: 205 MPa, 380 MPa, and 25%, respectively (Matweb 2019a).

For the cast-iron tensile results, there is significant variability in the curves. However, within each chemistry and source, mechanical behaviors were consistent, meaning each ingot is relatively homogenous. Due to a lower C equivalence, it was expected that the third Bosch C cast iron would have shown a greater tensile strength (Davis 1996). The cooling rate of cast iron has been shown to affect the mechanical properties of the casting, with higher cooling rates giving higher strength material (Behnam et al. 2010). Due to the cooling rate variability throughout each ingot dependent on pouring speed, initial solidification location in the mold, etc., these results are highly susceptible to differences amongst iterations of the same material. The primary cause of the variance in the cast iron tensile results is likely cooling rate variation and dendrite formation differences between each casting (Collini et al. 2008). The two different C sourced alloys showed similar tolerance in the tensile curves, with the Bosch C results showing less consistency and the control ingots resulting in overall higher fracture stresses with a tighter grouping of the three ingots.

The experimental results presented herein indicate internal consistencies within each ingot but do show variation between ingots. This is in agreement with the work published by Collini et al. (2008) where they document the significant variability of as-cast mechanical properties between one casting and the next, even when

(a)   (b)
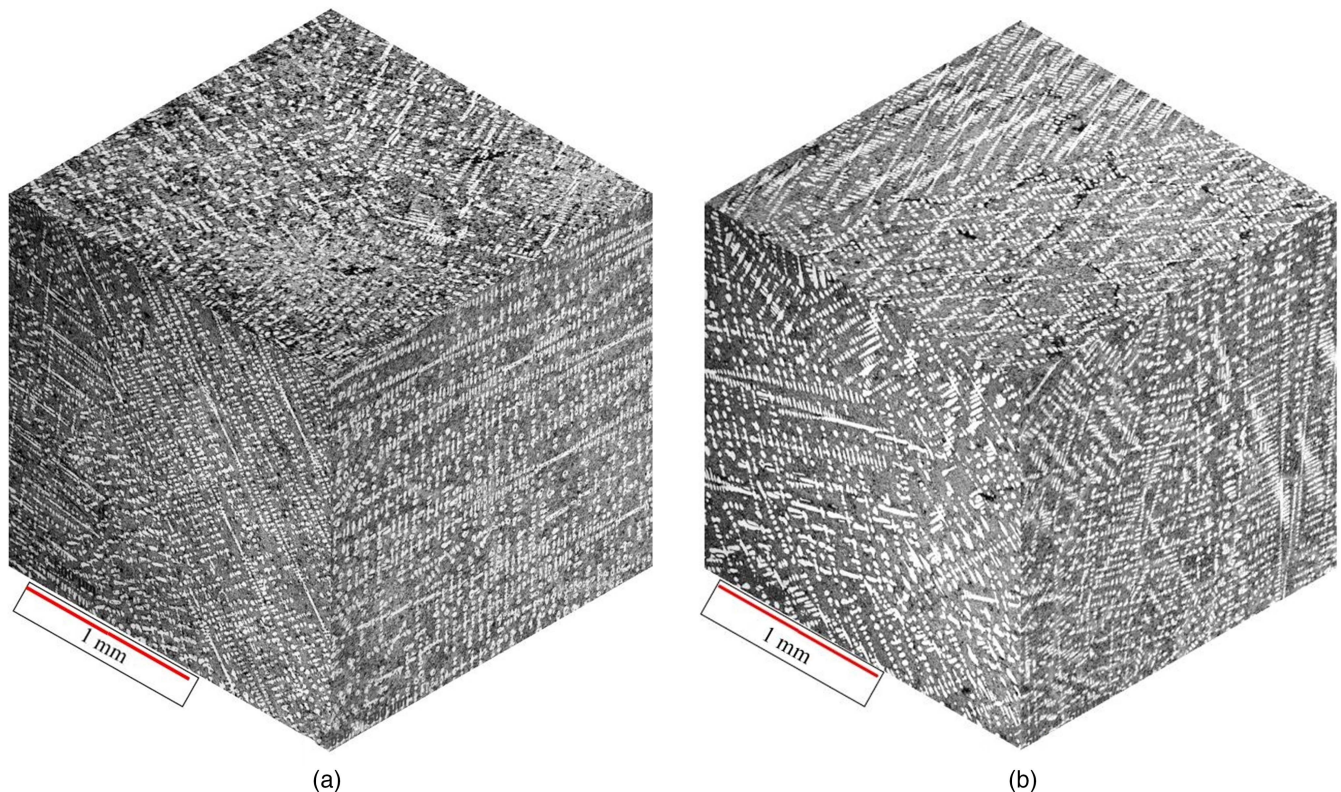
Fig. 7. Three-dimensional images constructed from two-dimensional micrographs of cast iron using: (a) control C source; and (b) Bosch C source.
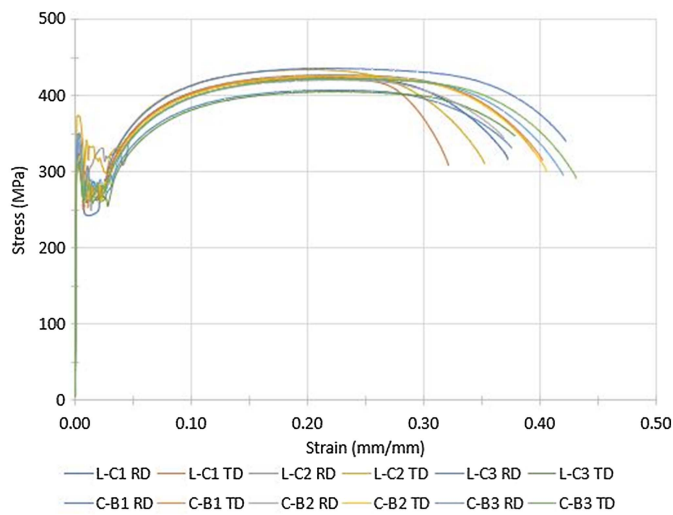
Fig. 8. Tensile stress-strain curves obtained from low-C steel samples. L-C = control and L-B = Bosch. Curves are for both rolling direction (RD) and transverse direction (TD), strain-rate controlled at 0.001/s.
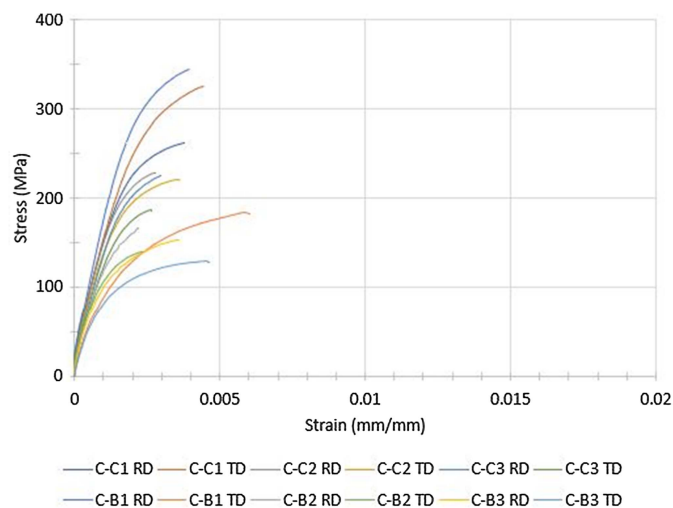
Fig. 9. Tensile stress-strain curves for cast-iron samples. C-C = control and C-B = Bosch. Curves are in both RD (pouring direction) and TD, strain-rate controlled at 0.001/s.

using near-identical initial conditions during casting (Collini et al. 2008). Such is the case with the casting results presented previously and subsequently, where the ingots were subjected to nominally identical conditions, with deviations between ingots being potentially caused by changes in respective cooling conditions (such as ambient temperature or humidity). In order to curtail uncertainty and homogenize material properties, cast components are often postprocessed through annealing/normalizing heat treatments, which would occur at approximately 800°C–900°C for 1-h per 2.5-cm (1-in.) thickness (Avcı et al. 2009).

The primary scope of the presented work is centered around the use of casting as a means for production of components in extraterrestrial environments, particularly on the Martian surface. Given the acute shortage of energy and resources in such environments, postprocessing of cast components through normalizing/annealing heat treatments would not likely be unfeasible owing to the significant energy and material costs associated with the process. Thus, the nonnormalized properties of the material should be observed.

In the case of a net-shaped casting of an object with complex features, spatial variation in microstructure and mechanical properties would be a function of local cooling rates, which would in turn be a function of local geometry. Because the geometry is determined by the required dimensions of the component and cannot be changed, it becomes imperative to establish bounds on the expected range of properties. Furthermore, of all the data gathered for the six total cast-iron ingots, the disparity was shown between the iterations of both C sources and not in the experimental Bosch C alone. This again shows the sensitivity of gray cast-iron production, which would lead to potential limits upon applications of the alloy as well as more stringent constrains on manufacturing conditions.

Fracture surfaces obtained from low-C steel tensile specimens are shown in Fig. 10. Fractography from low-C steel revealed ductile failure as shown by the significant plastic deformation.

These fracture surfaces show similar tensile characteristics for both C sources. Closer inspection of the low-C steel tensile specimens, shown in the SEM images in Fig. 11, reveal ductile, dimpled fracture surfaces from the void decohesion.

Fracture surfaces obtained from the cast-iron tensile specimens are shown in Fig. 12. The cast iron failed with sudden, brittle fracture with no visible plastic deformation with little strain. There is no discrete disparity between samples produced with different carbon sources at this level of magnification.

The cast-iron tensile samples failed less consistently; however, results were consistent within each ingot. After brittle fracture, closer inspection showed mostly graphite decohesion for both C sources in Fig. 13, similar to those found by previous studies (Bermont and Castillo 2003).

Compression tests were carried out to the limitations of the test machine or until fracture to present the performance similarities at further strain rates. For all low-C steels, the applied compressive load reached the maximum 82-kN load for every test without fracture. As shown in Fig. 14, the low-C steels exhibited an upper yield strength before a load drop off, giving a distinct yield point. Although these low-C steel samples did not reach an ultimate compressive stress point, each test resulted in a permanently distorted, barreled specimen indicative of a ductile material. The low-C compression plot shows near-identical performance for all low-C steel samples tested for both C samples.

All but two of the cast-iron samples (both samples from the first control C cast-iron ingot) fractured before reaching the upper load limit as set, giving a clearly defined failure point. As shown in Fig. 15, each specimen showed a sharp load drop where the ultimate compressive stress of the cast-iron materials is defined.

The cast-iron compression tests show significant variance in the data curves. This again directs attention to the need to control the cooling rate for cast iron if an annealing, normalization, or other heat-treatment process is not to be used, due to inconsistent microstructural formation in the as-cast condition. However, it is apparent that the Bosch C source showed tighter grouping of the stress-strain curves for the compression tests. Due to the fine particle size of the Bosch C, it is possible that the diffusion of C throughout the material was faster, giving a more homogeneous material; however, this is strictly speculation.

All hardness test results are given in Table 4. For the low-C steels, hardness deviation between the control and Bosch C alloys is minimal for Brinell (BHN) and Rockwell-B (HRB) scale. The average hardness for AISI 1020 steel is around BHN111 (Matweb 2019a), very close to the average BHN116 for conventional low-C and BHN113 for the Bosch low-C steels that were obtained here.

The cast-iron BHN results are significantly higher for the first control C cast-iron ingot, which causes the deviation to be inflated.

Table 3. Tensile testing results for all materials cast

Materials	Ingot ID	Young's modulus, E (GPa)	Upper yield stress, σ_{uys} (MPa)	Lower yield stress, σ_{lys} (MPa)	Ultimate stress, σ_{uts} (MPa)	Fracture stress, σ_{fs} (MPa)	Total elongation in gauge length (%)
Low-alloy steel, conventional C	1	221	336	276	424	304.5	36
	2	205	285	300	430	302	39
	3	201	333	261	406	282	41
	Average	**209 ± 11**	**351 ± 29**	**279 ± 20**	**420 ± 12**	**296 ± 13**	**39 ± 3**
Low-alloy steel, Bosch C	1	223	342	279	432	308	43
	2	217	340	277	422	294	42
	3	211	349	275	422	292	43
	Average	**217 ± 6**	**344 ± 5**	**277 ± 2**	**425 ± 6**	**298 ± 9**	**42 ± 0.2**
Cast iron, conventional C	1	119	N/A	N/A	284	284	0.4
	2	110	N/A	N/A	227	226	0.3
	3	99	N/A	N/A	213	212	0.3
	Average	**109 ± 10**	**N/A**	**N/A**	**241 ± 38**	**240 ± 38**	**0.3 ± 0.1**
Cast iron, Bosch C	1	119	N/A	N/A	293	292	0.5
	2	84	N/A	N/A	168	168	0.3
	3	65	N/A	N/A	146	144	0.4
	Average	**89 ± 27**	**N/A**	**N/A**	**202 ± 79**	**201 ± 79**	**0.4 ± 0.1**

Note: Bold represents the averages.
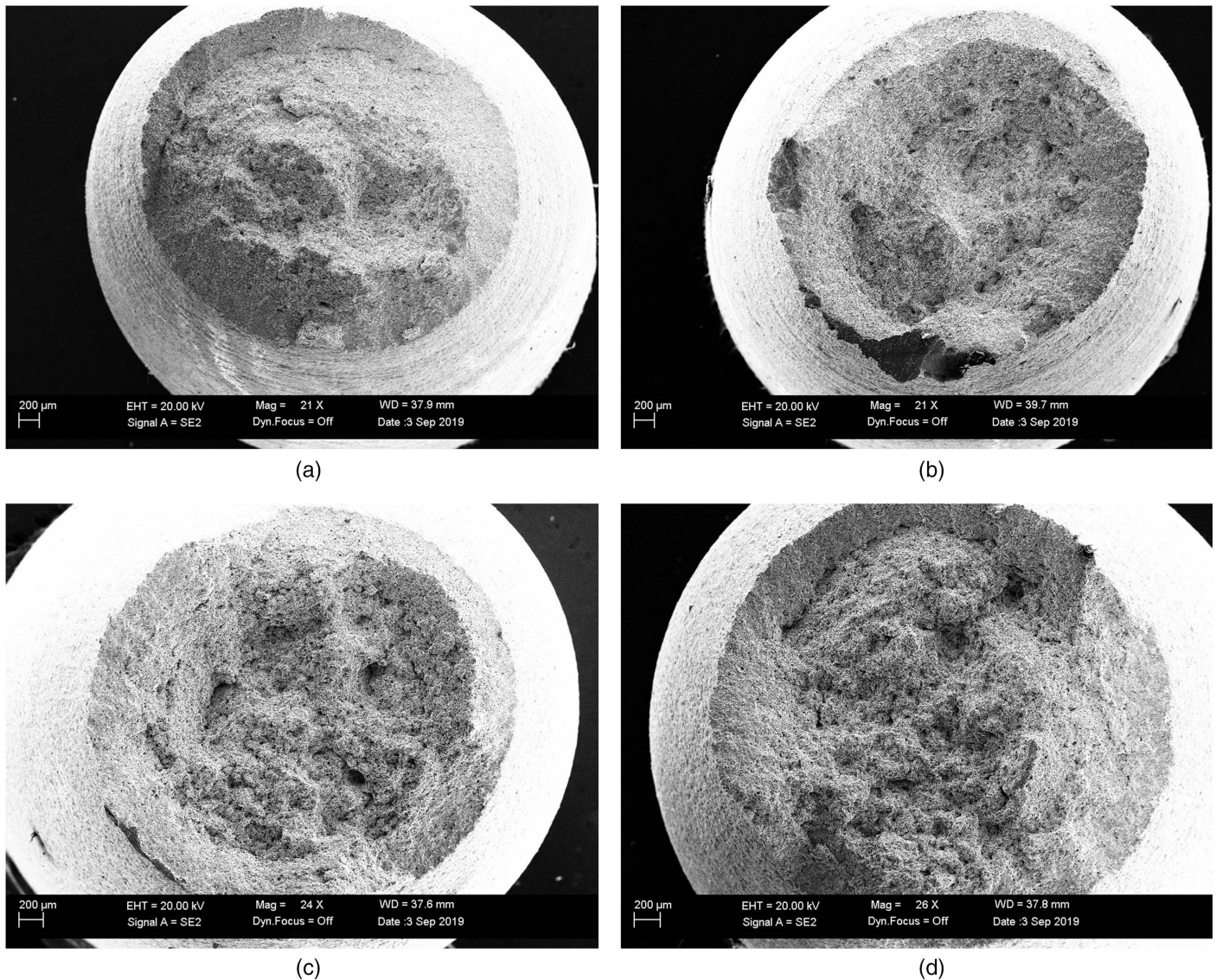
Fig. 10. SEM micrographs obtained from tensile tested low-C steels produced using (a and b) conventional C tested along transverse direction; and (c and d) Bosch C tested along rolling direction.
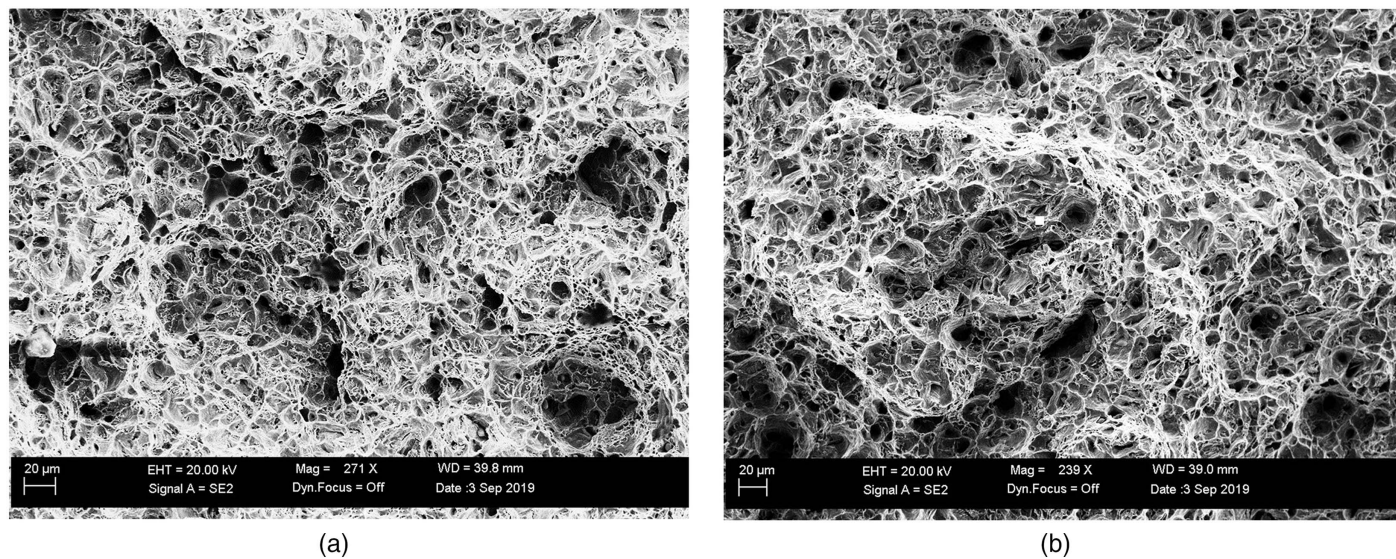
Fig. 11. SEM micrographs of fracture surfaces obtained from the low-C steels in the transverse direction produced using: (a) conventional C source; and (b) Bosch C source.
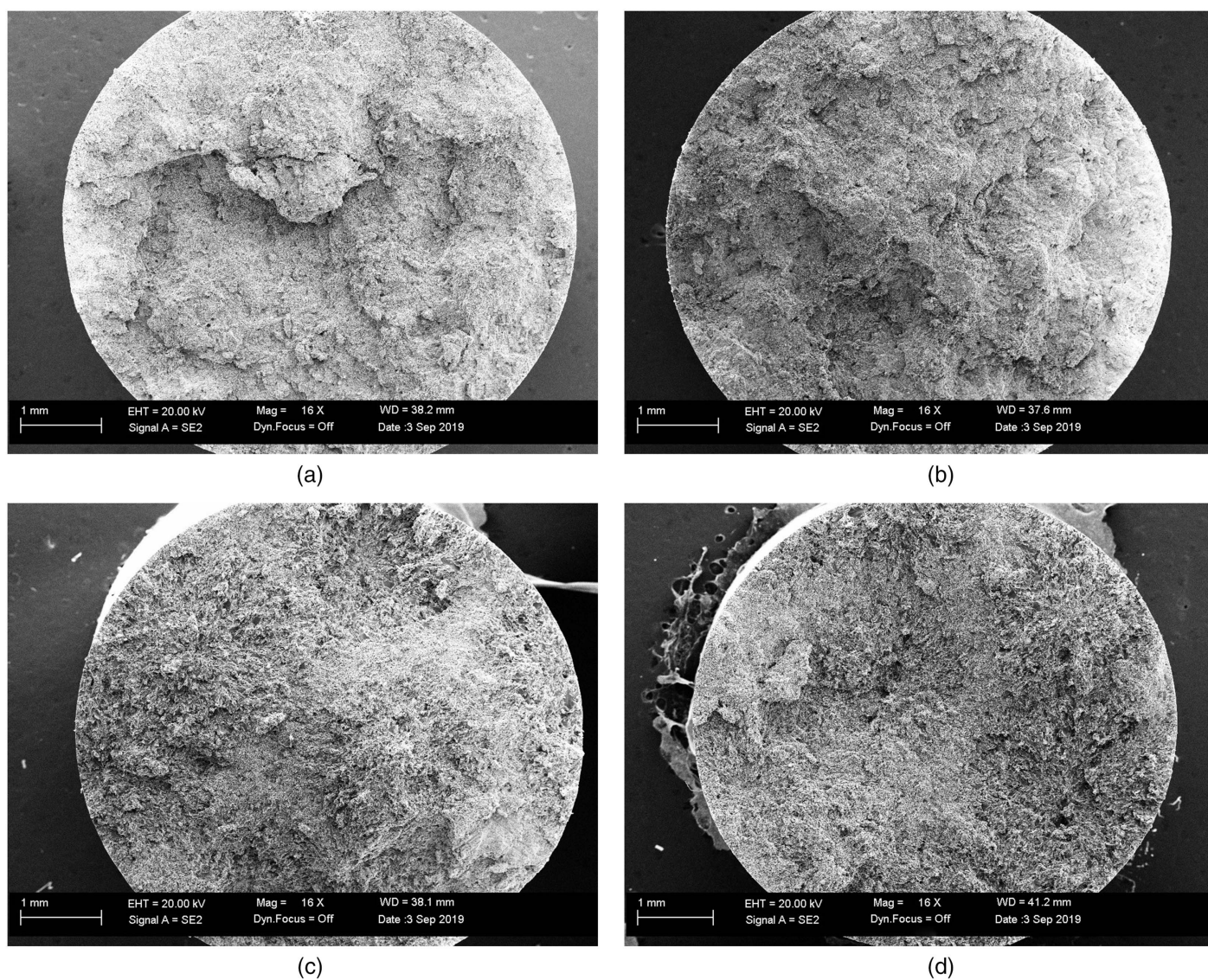
Fig. 12. SEM micrographs obtained from tensile tested cast iron produced using (a and b) conventional C tested along transverse direction; and (c and d) Bosch C tested along casting direction.
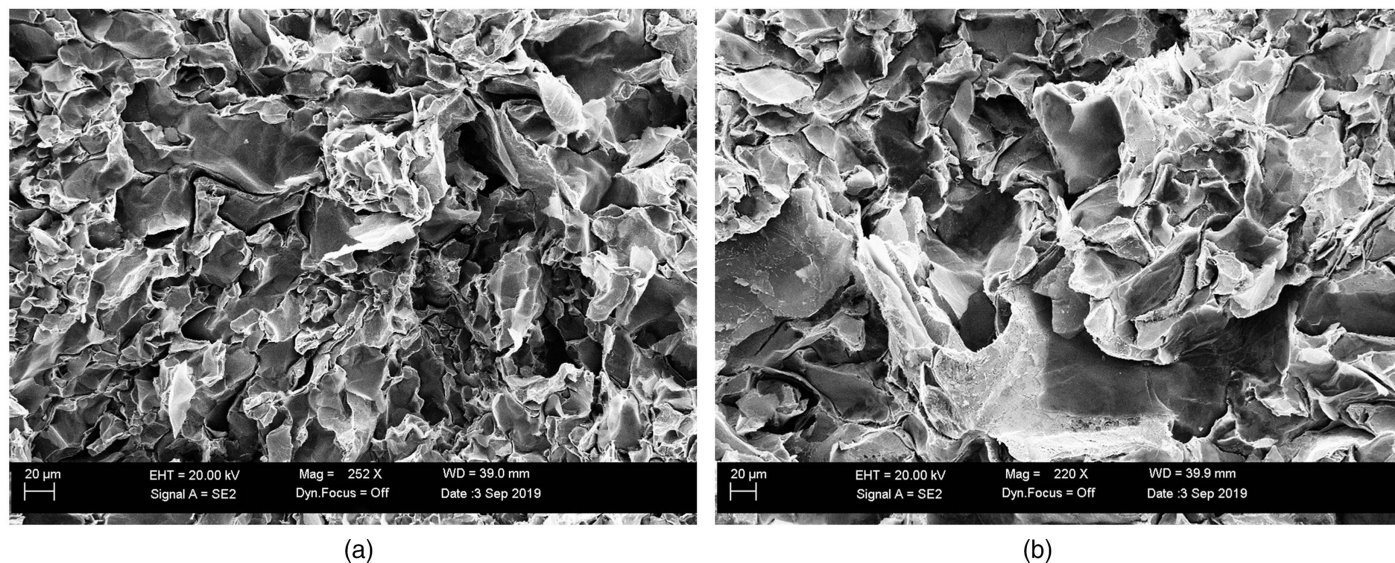
Fig. 13. SEM micrographs of fracture surfaces obtained from the cast iron in the transverse direction produced using: (a) conventional C; and (b) Bosch C.
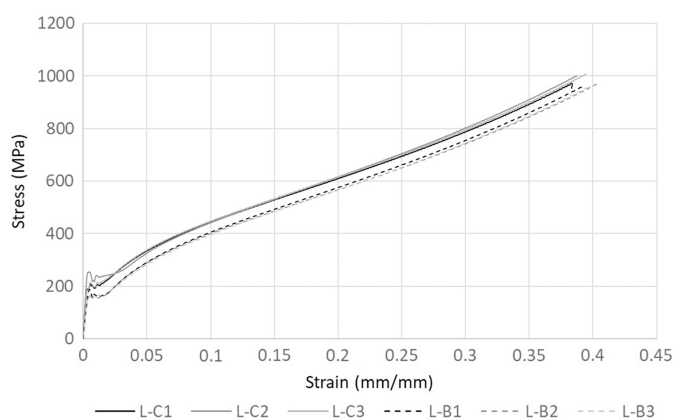
Fig. 14. Compressive stress-strain curves for low-carbon samples. C-C = control and C-B = Bosch. Strain-rate controlled at 0.001/s.
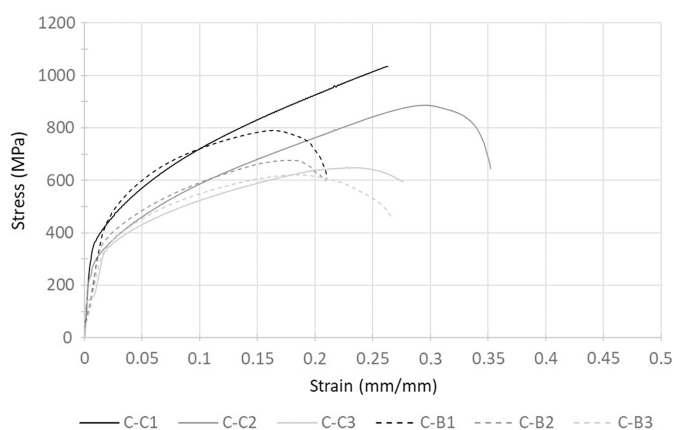
Fig. 15. Compressive stress-strain curves obtained from cast irons. C-C = control and C-B = Bosch. Strain-rate controlled at 0.001/s.

This ingot was tested numerous times in multiple locations, each reading in the BHN249 range. However, HRB and HRC tests showed low deviation across the cast-iron ingots, including the first control cast-iron ingot. It was expected that the hardness of the second control C cast iron would have been slightly lower due to the variation in Si content (El-Sawy et al. 2017; Atanda et al. 2011). The gray cast iron that was cast for this study was chosen as an average representative chemical composition target based on gray cast iron. Overall, the expected hardness for this material can range from BHN120 to 550 (HRC11.4 to 29). This material is similar in composition to SAE J431 automotive gray cast iron (Matweb 2019b), which expects a hardness of less than BHN187.

Apart from the first control C ingot, all cast irons had results within this parameter. The first ingot could have obtained a faster cooling rate than the other ingots, resulting in higher hardness values. It has been shown that cooling rate, when fast enough, can increase hardness significantly due to the formation of white iron within the gray iron matrix (Behnam et al. 2010). It is unlikely that the source of the C used in alloying played a significant role in the hardness variation. Overall, hardness values obtained from samples manufactured using different C sources showed comparable mechanical properties.

Overall, the low-C steel alloys showed easily comparable structure and properties for both C sources. The cast-iron alloys again showed some differences in the structure and mechanical testing performed here. These differences are not only seen when comparing two C sources, but also when looking at the different iterations of the each material grade. However, each ingot showed relatively consistent data in comparison to their own test specimens. Based on the similarities in material properties for both alloys, this suggests that the Bosch C could be used not only for multiple alloys, but also for a range of steels whose properties are modified by cooling rate control or postsolidification processing such as heat treatments or forging.

However, if a cast-iron component is desired to be used in the as-cast state, the properties found for a cast-iron component can easily vary depending on geometry and section thickness, causing significant variability in local properties throughout a part (Collini et al. 2008). Due to cooling rate differences in an as-cast part

Table 4. Hardness test results all materials cast

Materials	Ingot ID	Hardness		
		BHN	HRB	HRC
Low-carbon steel, conventional C	1	111	54.0	N/A
	2	123	68.6	N/A
	3	114	57.8	N/A
	Average	**116 ± 6**	**60.1 ± 8**	**N/A**
Low-carbon steel, Bosch C	1	109	58.0	N/A
	2	111	60.5	N/A
	3	119	64.2	N/A
	Average	**113 ± 5**	**60.9 ± 3**	**N/A**
Cast iron, conventional C	1	249	82.8	5.6
	2	162	81.4	3.2
	3	167	85.2	4.6
	Average	**193 ± 49**	**83.1 ± 2**	**4.5 ± 1**
Cast iron, Bosch C	1	175	84.5	4.2
	2	163	80.9	2.2
	3	163	83.1	2.2
	Average ± standard deviation	**167 ± 7**	**82.8 ± 2**	**2.9 ± 1**

Note: Bold represents the averages.

attributed to environment, mold conditions, pouring speed, and others, the microstructure of as-cast gray iron is likely to result in significant variation in mechanical properties. Cast iron is also often tested in the form of test bars, which could give less variability across the casting versus an ingot mold like the ones used here; however, that capability was not possible at the time of this study. To minimize these internal variations, a normalization, annealing, or other heat-treatment process could be used for cast iron to ensure the ingots present less variability from each iteration.

Conclusion

Two different types of ferrous alloys, a low-C steel similar to AISI 1020 and a gray cast iron, were manufactured by using a conventional C and Bosch-sourced C. Mechanical and microstructural investigation results obtained from each equivalent material revealed comparable metallurgical properties. The variations for this study are not attributable to the difference in C source. The results indicate that it is possible to use the Bosch-sourced C as the elemental C alloying source in steelmaking.

Data Availability Statement

Some or all data, models, or code that support the findings of this study are available from the corresponding author upon reasonable request, including raw material, charge calculations, castings compositions, micrographs, hardness, SEM and XRD, and mechanical testing data.

Acknowledgments

References

Abney M. B., T. Komas, and J. Alleman. 2016. "Using NASA life support technology to reduce cement industry CO2 emissions and explore improvements to concrete durability." In *Proc., ACI Strategic Development Council #40*. Salt Lake City: American Concrete Institute.

Abney, M. B., J. Mansell, C. Stanley, J. Edmunson, S. DuMez, and K. Chen. 2013. "Ongoing development of a series Bosch reactor system." In *Proc., 43rd Int. Conf. on Environmental Systems*. Portland, OR: American Institute of Aeronautics and Astronautics.

Abney, M. B., and J. M. Mansell. 2011. "Evaluation of Bosch-based systems using non-traditional catalysts at reduced temperatures." In *Proc., 41st Int. Conf. on Environmental Systems*. Portland, OR: American Institute of Aeronautics and Astronautics.

ASTM. 2013. *Standard test methods for determining average grain size*. ASTM E112-13. West Conshohocken, PA: ASTM.

ASTM. 2016. *Standard test methods for tension testing of metallic materials*. ASTM E8/E8M-16a. West Conshohocken, PA: ASTM.

ASTM. 2018. *Standard specification for plates, carbon steel, structural quality, furnished to chemical composition requirements*. A830/A830M-18. West Conshohocken, PA: ASTM.

ASTM. 2019a. *Standard test method for evaluating the microstructure of graphite in iron castings*. ASTM A247-19. West Conshohocken, PA: ASTM.

ASTM. 2019b. *Standard test methods of compression testing of metallic materials at room temperature*. ASTM E9-19. West Conshohocken, PA: ASTM.

Atanda, P., G. Oluwadare, and L. Oluwole. 2011. "Effect of silicon content and shake-out time on hardness and grain size properties of GL 250 cast iron." *J. Miner. Mater. Charact. Eng.* 10 (3): 257–266. https://doi.org/10.4236/jmmce.2011.103017.

Avcı, A., N. İlkaya, M. Şimşir, and A. Akdemir. 2009. "Mechanical and microstructural properties of low-carbon steel-plate-reinforced gray cast iron." *J. Mater. Process. Technol.* 209 (3): 1410–1416. https://doi.org/10.1016/j.jmatprotec.2008.03.052.

Behnam, M. J., and P. Davami, and N. Varahram. 2010. "Effect of cooling rate on microstructure and mechanical properties of gray cast iron." *J. Mater. Sci. Eng. A* 528 (2): 583–588. https://doi.org/10.1016/j.msea.2010.09.087.

Bermont, V., and R. Castillo. 2003. "Qualitative and quantitative studies of fracture surfaces in ductile and grey cast irons." *Int. J. Cast Met. Res.* 16 (1–3): 257–262. https://doi.org/10.1080/13640461.2003.11819592.

Collini, L., G. Nicoletto, and R. Koecna. 2008. "Microstructure and mechanical properties of pearlitic gray cast iron. *J. Mater. Sci. Eng. A* 488 (1–2): 529–539. https://doi.org/10.1016/j.msea.2007.11.070.

Cullity, B. D.,, and S. R. Stock. 1978. *Elements of X-ray diffraction*. Reading, MA: Addison-Wesley.

Davis, J. R. 1996. *ASM specialty handbook—Cast irons*. Materials Park, OH: ASM International.

Devi, T., and M. Kannan. 2007. "X-ray diffraction (XRD) studies on the chemical states of some metal species in cellulosic chars and the Ellingham diagrams." *Energy Fuels* 21 (2): 596–601. https://doi.org/10.1021/ef060395t.

Dieter, G. E. 1986. *Mechanical metallurgy: Strengthening mechanisms*, 197–201. Boston: McGraw-Hill.

El-Sawy, E., M. El-Hebeary, and I. El Mahallawi. 2017. "Effect of manganese, silicon and chromium additions on microstructure and wear characteristics of grey cast iron for sugar industries applications." *Wear* 390–391. https://doi.org/10.1016/j.wear.2017.07.007.

Erickson, K., and H. Doyle. 2019. "How far away is the Moon?" Accessed May 17, 2021. https://spaceplace.nasa.gov/moon-distance/en/.

Esrafilzadeh, D., et al. 2019. "Room temperature CO_2 reduction to solid carbon species on liquid metals featuring atomically thin ceria interfaces." *Nat. Commun.* 10 (1): 1–8.

Kramer, S., and D. Mosher. 2016. "Here's how much money it actually costs to launch stuff into space." *Insider*, July 20, 2016.

Mahaffy, P., et al. 2013. "Abundance and isotopic composition of gases in the Martian atmosphere from the Curiosity rover." *Science* 341 (1): 263–266. https://doi.org/10.1126/science.1237966.

Matweb. 2019a. "AISI 1020 Steel, hot rolled, 19-32 mm (0.75-1.25 in) round." Accessed September 10, 2019. http://www.matweb.com/search/DataSheet.aspx?MatGUID=b58ee61a3745453a9232f7864abba74f.

Matweb. 2019b. "SAE J431 automotive gray cast iron, SAE grade G1800." Accessed September 10, 2019. http://www.matweb.com/search/DataSheet.aspx?MatGUID=7fb051b85b4c4b5295e6a6a45bf6fa33.

NASA (National Aeronautics and Space Administration). 2020. "Mars in our night sky." Accessed May 17, 2021. https://mars.nasa.gov/all-about-mars/night-sky/close-approach/.

Radzikowska, J. M. 2004. "ASM handbook." In Vol. 9 of *Metallography and Microstructures of cast iron*. Materials Park, OH: ASM International.

Smith, W. F., and J. Hashemi. 2006. *Foundations of materials science and engineering: Mechanical properties of metals I*, 254–255. New York: McGraw-Hill.

Zafar, R. 2020. *SpaceX could bring starship launch costs down to $10/kg believes Musk*. London: Wccftech.